

Soft Matter

ELECTRONIC SUPPLEMENTARY INFORMATION

Growth of gas-filled penny-shaped cracks in decompressed hydrogels

Yansheng Zhang^a, Merlin A. Etzold^a, Adrien Lefauve^{a,‡}

In this ESI we complement the information given in the main paper regarding our measurement of the super-saturation pressure p_s (§ 1), our measurement of the Young elastic modulus E (§ 2), our image acquisition and analysis (§ 3), and our estimation of the importance of axial vs radial diffusion of dissolved gas (§ 4).

1 Pressure p_s measurements

1.1 Protocol and pressure reading error

The experimental temperature is maintained at $23 \pm 2^\circ\text{C}$ by a room air-conditioning system turned on several hours before decompression. The actual water temperature T was always measured in each experiment with an alcohol thermometer (to 0.5°C accuracy) prior to the imaging, and was used for the quantitative results.

After > 48 hours of swelling of the hydrogels, and hours of thermal equilibrium, the seal cap* on the bottle was opened and swapped for a pressure measurement cap. This ‘cap swap’ was necessary due to (i) the limited number of pressure gauges available and our need to run experiments in batches using several bottles; (ii) the imperfect seal provided by pressure gauges which would have caused unacceptable pressure loss during the long swelling time of the beads. The bottle was then vigorously shaken to re-establish equilibrium between the pressurised gas (CO_2) pocket and the liquid phase below it. Two tubes were connected to this pressure measurement cap.

The first tube was connected to a small pressure gauge, which had a wide range but was relatively inaccurate. It was used to give a rough estimate of the gas pressure in the bottle, so that a more suitable gauge (in terms of range and resolution) could then be chosen for a more accurate measurement.

The second tube was connected to a closed valve. The most appropriate pressure gauge chosen above was then attached to

this valve, and the valve was opened to connect the gauge to the bottle and get a pressure reading.

Two pressure gauges were used in the experiment: one with 2.5 bar range, and one with 4 bar range (both relative to atmospheric pressure p_a), with respective resolution of ± 0.05 bar and ± 0.1 bar, i.e. around $\pm 2\%$ of their maximal value. To be conservative, we consider that any single pressure reading $p_s - p_a$ is prone to a fixed $\pm 5\%$ error.

Next, we discuss how we used this reading to estimate the actual gas pressure before the cap swap (§ 1.2) and therefore the associated dissolved gas concentration in the hydrogel, which is of greatest importance in our model (§ 1.3).[†]

1.2 Cap swap leak correction

Introduction. Here we comment on the issue, sketched in figure 1, that a small amount of CO_2 would leak out of the system during the cap swap (figure 1b). This caused our measured value of the CO_2 pressure p_s^1 after the cap swap (figure 1c) to underestimate the ‘real’ one during the swelling of the bead, that we call $p_s^0 \gtrsim p_s$ (figure 1a).

Note, however, that the loss due to cap swap does not affect the CO_2 concentration within the hydrogel beads, which remains equal to $c_s^0 = k_h p_s^0$, as there is insufficient time for CO_2 to diffuse out of the bead (diffusion with a constant of order $D \sim 10^{-9} \text{ m}^2 \text{ s}^{-1}$ only penetrates into the bead by a negligible thickness $\sim \sqrt{Dt} \approx 10^{-4} \text{ m}$ over a duration 10 s). Our objective is therefore to estimate p_s^0 .

Dominant mechanism. There are two mechanisms contributing to the loss of CO_2 during the cap transfer.

First, the CO_2 gas initially present in the pressurised gap[‡] (panel a) is released when the seal is broken (panel b). When p_s is measured, CO_2 gas comes out of the solution to re-pressurize

^a Department of Applied Mathematics and Theoretical Physics, University of Cambridge, Wilberforce Road, Cambridge CB3 0WA, United Kingdom.

[‡] Corresponding author. Email: lefauve@damtp.cam.ac.uk.

* The seal cap was a ‘tamper evident’ screw cap designed for new soda bottles, i.e. with an additional security ring offering excellent seal.

[†] In the following discussion we always mention the specific gas (CO_2) used in all our experiments. This is done merely for convenience, but our calculations and discussion can be applied without loss of generality to any pure gas (e.g. replacing ‘ CO_2 ’ by ‘ N_2 ’ everywhere except when actual specific constants like D, k_h are needed).
[‡] Note that any air (N_2, O_2) introduced in the gap will be purged by CO_2 bubbling out of solution, such that we assume that the pressurised gap is always pure CO_2 .

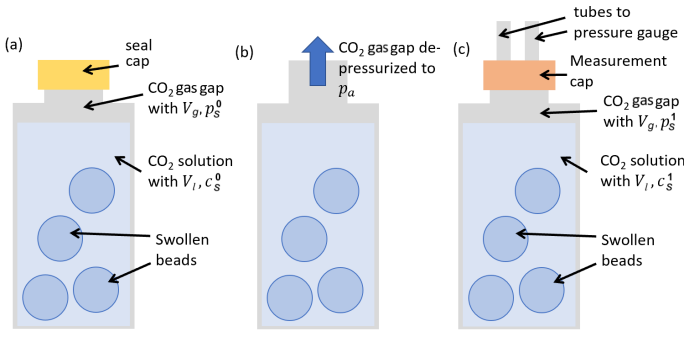


Fig. 1 Illustration of the cap swap leak and its associated source of error. System (a) during the swelling of the hydrogel beads; (b) during the cap swap; (c) during the first pressure measurement.

the gap and establish a new equilibrium (panel c).

Second, when the pressure is released, CO₂ can bubble out directly out of solution. However, we estimate that this second mechanism is relatively insignificant as the bubbling is reasonably slow in experiments (probably due to very few available nucleation sites).

We therefore propose a correction for the amount of CO₂ lost during swapping the caps based on the first mechanism, which we assume to be dominant.

Conservation of CO₂. The volume of the gas gap inside the bottle is denoted V_g, and the liquid solution beneath it V_l (excluding the beads). The total amount of molecular CO₂ in the system (excluding the beads) after removal of the seal cap (panel b) is

$$n_{\text{panel b}} = \frac{p_a V_g}{RT} + c_s^0 V_l, \quad (1)$$

i.e. the sum of the gaseous and dissolved mole content.

After re-pressurization (panel c), we have $n_{\text{panel c}} = n_{\text{sol}} + n_{\text{gas}}$ where

$$n_{\text{sol}} = c_s^1 V_l \quad \text{and} \quad n_{\text{gas}} = \frac{p_s^1 V_g}{RT} = \frac{c_s^1 V_g}{k_h RT}, \quad (2)$$

where we recall that k_h is the Henry solubility constant.

By conservation of CO₂ from panel b to c we therefore have

$$\frac{p_a V_g}{RT} + c_s^0 V_l = c_s^1 V_l + \frac{c_s^1 V_g}{k_h RT}. \quad (3)$$

Correction factor. This can be re-arranged to find the required correction between p_s^0 and p_s^1

$$c_s^0 = k_h p_s^0 \quad \text{where} \quad p_s^0 = p_a + (p_s^1 - p_a) \left(1 + \underbrace{\frac{1}{k_h RT} \frac{V_g}{V_l}}_{\text{correction factor}} \right). \quad (4)$$

The correction factor is $\approx 1.18(V_g/V_l)$ at 25°C, and vanishes as $V_g/V_l \rightarrow 0$ (the ideal case, which could not be achieved experimentally, as it was difficult to reduce V_g below 50cm³ due to vigorous bubbling following the initial carbonation).

Validation and practical issues. We validated the principle behind this theoretical correction (4) by a set of *ad hoc* experiments in which we systematically varied V_g/V_l by varying the water level (measured by weighing the bottle) and measured the actual ra-

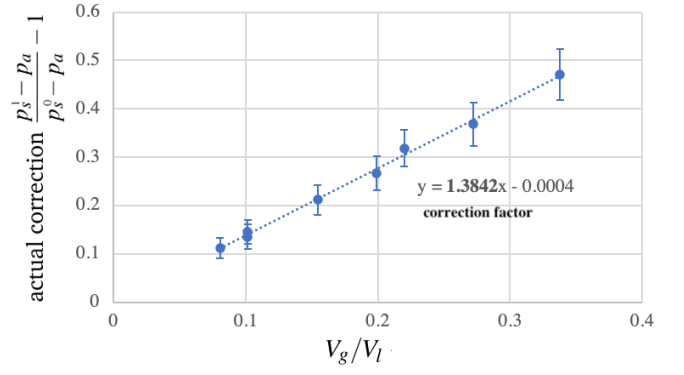


Fig. 2 Experimental validation of the pressure correction (4). Note that the slope of the fit (≈ 1.38) is slightly larger than expected (≈ 1.18). The intercept of the fit was adjusted to 0 by adding to V_g an *ad hoc* volume of gas corresponding to that in the pressure gauge and tubing, as well as the deformation of the plastic bottle under pressure. These practical issues led us to abandon this correction method directly based on (4) and adopt instead the final correction method shown in figure 3.

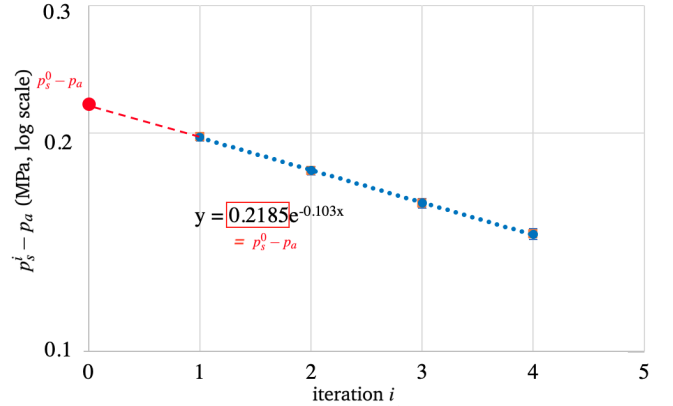


Fig. 3 Illustration of the final correction method to determine the pressure p_s^0 before the first cap swap (in red) based on an exponential extrapolation of the pressures p_s^i obtained after i iterations of the cap swap (in blue). This method relies on the theoretical expectation (4) but does not require us to input V_g/V_l, k_h , T , thus yielding very accurate results (here $p_s^0 - p_a = 2.185$ bar).

tio $(p_s^1 - p_a)/(p_s^0 - p_a) - 1$ (using a pressure measurement cap to measure p_s^0 , opening the bottle, closing it again, shaking vigorously, and measuring p_s^1). The results are shown in figure 2. The linear fit gives a correction factor $\approx 1.38(V_g/V_l)$, but obtaining a zero intercept required us to add to the ‘bottle’ V_g an additional *ad hoc* 23cm³ to account for (i) the ‘dead’ gas volume inside the pressure gauges and tubing, and (ii) the visible deformation of the plastic bottles under pressurisation.

The first correction method that we attempted consisted in computing p_s^0 from $p_s^1, V_g/V_l, k_h, T$ using the theoretical formula (4), much as sketched in figure 2 (we had typical values of $V_g/V_l \approx 0.15$). However, this method was not used in the final data plotted in figure 8 of the paper because of the discrepancy between predicted and actual correction factor, and the uncertainty about the extra gas volume due to the pressure gauge, tubing and bottle deformation.

Final correction method. Instead, we used a different and more robust correction method. Instead of measuring p_s^1 only once, we performed the cap swap procedure at least two more times (opening the bottle, closing it, shaking vigorously, measuring p_s^2 , etc) in order to obtain a series of measurements $p_s^1, p_s^2, p_s^3, p_s^4$, as shown in figure 3. The correction was then straightforward: we fitted a straight line through the set of points $\{(i, \log p_s^i)\}$ (in blue), and extrapolated to find $(0, p_s^0)$ (in red) with good accuracy (without requiring us to input $V_g/V_g, k_h, T$).

This method was used to correct for the predicted $\alpha = DS^2\ell^{-1}$ (in figure 8 of the main paper), which proves critical in our work because of the square dependence of $S^2 \propto (p_s^0 - p_a)^2$. In order to compute the error bars on the predicted α , the error on p_s^0 that we used was based on the standard error of this extrapolated fit (varying between 0.2–1%). This correction method therefore allowed us to determine p_s^0 with a smaller error than would have ever been possible by applying the theoretical correction (4) on a single pressure reading (which carried a $\pm 5\%$ error as explained above).

1.3 Gas-liquid equilibrium error

Finally, for completeness we mention a last plausible source of error in the estimation of the ‘real’ c_s^0 for the ‘real’ pressure p_s^0 .

Henry’s equilibrium. By using Henry’s law, we assume equilibrium between the liquid and the gas phase before each cap swap. This is not necessarily the case on the experimental time scale, since equilibrium is achieved by the nucleation of dissolved gas into small bubbles, which then rise to the surface to pressurise the gas gap. However any bubble nucleation (creating a gas/liquid interface) needs to overcome the surface tension γ (energy which effectively acts as an energy barrier). This can be expressed quantitatively using the statistical rate of homogeneous nucleation $\propto \exp\{-\gamma^3/\ln^2(p_s^{\text{curr}}/p_s^{\text{eq}})\}$, where $p_s^{\text{curr}}/p_s^{\text{eq}} \lesssim 1$ is the ratio of current to equilibrium pressures (see Ref. 1, equation 4). The ‘closer’ the system is to equilibrium ($p_s^{\text{curr}}/p_s^{\text{eq}} \rightarrow 1$), the ‘harder’ it becomes to spontaneously overcome this barrier (the rate of nucleation $\rightarrow 0$ and is very flat).

Nucleating agents. To overcome this barrier, ‘nucleating agents’ (usually sand or ceramic pieces) could be added to the solution to promote heterogeneous nucleation. This was attempted but not pursued further for two reasons. First, because nucleating agents scratched and damaged the hydrogel beads, making them susceptible to fracture from the surface (as opposed to internal fractures, the focus of the main paper). Second, because the gas bubbles forming on the nucleating agent at high pressure were so small that they could not spontaneously detach from its surface within a reasonable amount of time, rendering it ineffective.

Shaking. Therefore, we only promoted CO_2 nucleation by mechanical agitation, i.e. by vigorously shaking the bottle (but gently, so as not to damage the hydrogel beads inside). Pressure measurements were only taken after the pressure had reached a steady state. We believe that this allowed a sufficiently good equilibrium to be reached, and that this source of error was probably negligible, and certainly systematic.

2 Young modulus E measurements

Hertz contact theory. After the pressure measurements, the bottle was cut open to retrieve the beads (spherical with diameters around 25 mm). Their shape allowed for an easy measurement of the Young modulus using the Hertz contact theory (see Ref. 2 § 9, and Ref. 3). When two elastic spheres with radius R_1, R_2 , modulus E_1, E_2 and Poisson coefficient ν_1, ν_2 are pressed against each other, the contact forces depend on the total deformation h via

$$F = er^{1/2}h^{3/2} \quad (5)$$

where $1/r = 1/R_1 + 1/R_2$ and $e = \frac{4}{3}(\frac{1-\nu_1^2}{E_1} + \frac{1-\nu_2^2}{E_2})^{-1}$.

Practical application. Now consider the case of a single sphere with R, E, ν compressed against an inelastic plate modelled as $E_2 = \infty$ and $R_2 = \infty$. We identify $r = R$ and $e = \frac{4}{3} \frac{E}{1-\nu^2}$, and find the force as

$$F = \frac{4}{3} \frac{E}{1-\nu^2} R^{1/2} h^{3/2} \quad (6)$$

Letting $k_0 = \frac{4}{3} \frac{E}{1-\nu^2} R^{1/2}$, we invert and write $h = k_0^{-2/3} F^{-2/3}$.

In our setup, sketched in figure 4, compression occurred both on top and at the bottom. If the force measured by the force sensor is F_m , then the total compression is given by

$$h_{\text{tot}} = k_0^{-2/3} (F_m^{-2/3} + (F_m + W)^{-2/3}) \quad (7)$$

where W is the weight of the bead.

Protocol. During the experiment, the bead was first placed on a 0.01 g balance without the top touching the upper glass surface. This gave a bead mass reading m , which was used to calculate the radius of the bead (assuming a density of 1000 kg m^{-3}). Next, the balance was tared, the translation stage was slowly raised, and the vertical translation d of the stage was recorded. Data were only acquired after the bead touched the top surface.

To obtain E , the d was fitted to F_m via $d = k_1(F_m^{-2/3} + (F_m + W)^{-2/3}) + b$ using ‘NonlinearModelFit’ in Mathematica (the code can be downloaded from the repository doi.org/10.17863/CAM.60212). Typically, data were taken at $250\mu\text{m}$ interval up to a compression of 2.5 mm on top of the compression due to the mass of the bead alone. The total time of the experiment was a few minutes at most, much less than the poro-elastic time scale of the bead.⁴ Also note that when the bead was compressed for a short period of time ($\approx 20\text{s}$), only a very small drop in the force reading was observed (approx 0.1 g on the balance), which we attribute to the surface wetting (explained below) rather than stress relaxation.

Results and errors. Typical results are shown in figure 5. The best-fit E value (here $E = 16658 \text{ Pa}$) reproduces the data very well. The fit typically has a very low standard error (of order 1%), which we determined for each experiment and plot as error bars in the main paper.

We also verified that measuring E after the end of an experiment (in the presence of an internal gas-filled crack) did not significantly change E . For the bead shown in figure 5, we found $E = 16546 \text{ Pa}$, i.e. less than 1% difference. However, E was always measured prior to the internal cracking for better accuracy

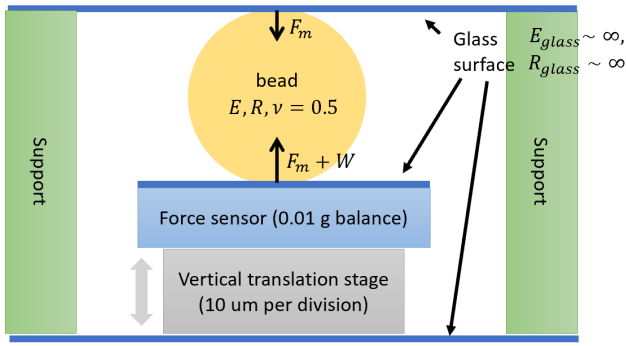


Fig. 4 Setup for measurement of the Young modulus E .

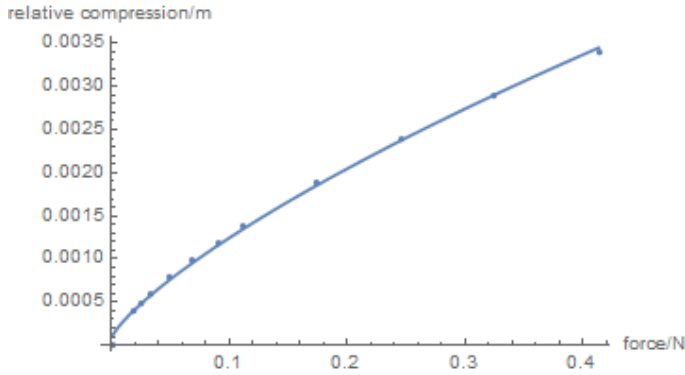


Fig. 5 Fitting of force/compression data to obtain E , here shown in a typical experiment giving $E = 16658 \text{ Pa}$.

and consistency.

For completeness we mention a potential source of error, which proved negligible in our measurements. Hydrogel beads are (of course) wet on the surface, which cannot be dried reliably because water would continually exude via osmosis. As a result, the glass surface is inevitably wetted when the bead is placed on it. On the upper surface this results in a slight upward surface tension force, reducing the mass reading on the balance (sometimes causing a negative reading of order 0.3 g, although a negative reading is taken to be zero in our data). However, we neglected this capillary force in our measurement since the other forces involved (F_m and $F_m + W$) are much larger.

3 Image acquisition and processing

3.1 Acquisition

The Canon XC10 4K camcorder was supported by a tripod that allowed the lens to point vertically downwards, about 1 m above the bead (with aperture f8-f10). As the camera was placed far away and had a long focal length (150–200 mm), it approximated an orthographic camera reasonably well (with an angle deviation of $< 3^\circ$ computed from the focal length and the XC10 sensor size $13.2 \text{ mm} \times 8.8 \text{ mm}$).

Our mirror system employed four mirrors at 45° from each other about to create four distinct ‘virtual horizontal’ views. The mirrors were supported by a 3D-printed holder designed specifi-

cally for our setup, using photo-sensitive resin at a high resolution of 0.1 mm, ensuring precise alignment. The mirrors were cut into a specific trapezium shape to make the setup more compact (to minimize perspective errors) while ensuring a sufficient field of view.

3.2 Contour fitting and filtering

The objective of our image analysis was to reliably extract the contours of the crack from each of the views (see figure 3a-d in the main paper). All image processing codes used below can be downloaded from the repository doi.org/10.17863/CAM.60212.

Background subtraction and binarisation. An early frame in the video was taken as the background frame for subsequent subtraction. The background frame had to be taken after the bead has been placed in the water tank because the bead itself introduces some difference to the original background due to its optical absorption and the imperfect matching of refractive indices.

Image were then binarised with a threshold set manually, which needed adjustment only in the rare cases when dust particles on the water surface floated into the field of view.

Contour detection. Contours were then detected in the binarised image. Conventionally, a cycle of erosion and dilation would be performed on the binarised image before contour detection in order to reduce noise, but this was not done here since we strived to achieve pixel resolution. Instead, we first computed a dilation of the polygon formed by the convex hull of the detected contours from the previous frame, and used it as a mask to block out anything far away from the crack.

Next, the detected contours in the current frame were filtered by their area. Any contour with an area less than a critical area of 20 Pixel^2 was ignored, and the rest of the contours formed a list of points which were fed into the ellipsoid fitting algorithm in the next stage. The contour detection algorithm was implemented using the robust Python interface ‘OpenCV’⁵, achieving near pixel resolution.

Finally, the calibration length-scale of the images (pixel to world coordinates) was obtained from the known diameter of the bead holder. The contours from each view were rotated upright using the vertical edge of the bead holder as a reference.

Two minor issues are worth mentioning. First, because the background frame was taken when the bead (with an internal crack) was already in water, some data would invariably be lost in the frames that immediately followed the background frame. This was because the crack would not grow sufficiently to generate sufficient image difference for the contour detection algorithm. Typically, 50 frames (corresponding to 2 s) immediately after the background frame were discarded. Second, the detected contours could be noisier when a view imaged almost directly the crack’s thin side (on the ‘edge’ rather than on the ‘face’ of the ‘penny’). This reduced image difference and negatively impacted contour detection. Typically, the binarisation threshold was reduced in such cases to ensure that the entire crack could be detected, but this inevitably introduced more noise in the contours (this error was quantified by sub-pixel averaging using our high temporal resolution, as explained in the main paper, and plotted

as error bars in figure 6b).

3.3 Ellipsoid fitting

Introduction. The theory of penny-shaped cracks predicts an axisymmetric ellipsoidal shape (i.e. with two major axes of equal radius R , also called a spheroid). This means that when the crack is projected onto different views, all detected contours are expected to be elliptical. The three-dimensional reconstruction of the crack was therefore based on the assumption that the crack was ellipsoidal in shape (although axisymmetry, i.e. the equality of the two major radii, was not enforced *a priori* to allow us to verify it). It was indeed verified *a posteriori* that this ellipsoidal shape turned out to be very accurate, as well as the axisymmetry (the two major radii were very nearly equal).

Our task was therefore to find the best fitting 3D ellipsoid, whose projections were closest to the detected contours in all four views in terms of squared error. However, least-squared fitting can be very sensitive to the noise in the contours detected in the previous stage. This requires us to first perform noise reduction (or filtering) on the detected contours.

Filtering (step 1). The detected contours from each view were first centered based on the center of mass of all the points on the contours. Next, the convex hull of each contour was computed and scaled to 80% of its original size. Any point inside the scaled convex hull was removed from contours. This effectively removed points that were clearly interior to the elliptical region (see figure 3e, step 1 in the main paper).

Filtering (step 2). Next, the remaining parts of the contours were fitted to the 2D ellipse equation ($ax^2 + 2bxy + cy^2 + dx + ey + f = 0$) using a least squared fitting algorithm.⁶ For each point, a residue (equal to the value of $ax^2 + 2bxy + cy^2 + dx + ey + f$) was computed, and half of points on the contours were discarded based on the residue value (see figure 3e, step 2 in the main paper). Finally, the remaining points were centered based on a further least squared ellipse fitting.

This represented a very strict filtering algorithm which gave good results most of the time, but which was unfortunately not always successful (when the detected contours were extremely noisy, we corrected manually).

Fitting. The four filtered and centered contours were finally used in the least squared fitting of a 3D ellipsoid, here arbitrarily centred at the origin $(x, y, z) = (0, 0, 0)$ (since its relative position and orientation in the bead was obtained but deemed irrelevant).

Such a 3D ellipsoid can be represented as a positive-definite matrix D with $x^T D x = 1$, allowing its projections on each imaging plane to be computed.⁷ The projected 2D ellipse were also similarly represented as a positive-definite matrix D' with $x^T D' x = 1$.

The error to be minimized was thus defined as $(x^T D' x - 1)^2 / l$ where l is the number of remaining contour points in the view considered. The errors from each of the views are summed and minimized using 'scipy.optimize.minimize' in Python.⁸ However, such a direct fitting required an initial guess to converge, which was generated by the method given in Ref. 7.

Finally, the projection of the fitted 3D ellipsoid using our al-

gorithm can be plotted with the remaining contour points after filtering to illustrate the goodness of the fit (see figure 3f in the main paper).

4 Axial vs radial diffusion

Here we give more details on the scaling arguments and numerical simulations performed to confirm the accuracy of our (purely axial) diffusion model.

Formulation. As explained in the main paper, the full (axisymmetric) two-dimensional diffusion problem for the gas concentration (in the medium surrounding a crack of negligible thickness) is complicated by the fact that the regions where Neumann and Dirichlet boundary conditions are imposed are changing continuously due to the expansion of the crack with a given $R(t)$. It is governed by the following system of equations in $(r, z) \in [0, \infty)^2$

$$\frac{1}{D} \frac{\partial c}{\partial t} = \frac{1}{r} \frac{\partial}{\partial r} \left(r \frac{\partial c}{\partial r} \right) + \frac{\partial^2 c}{\partial z^2} \quad (\text{axisymmetry}) \quad (8a)$$

$$c(r, z, t = 0) = c_b + \Delta c \quad (\text{initial condition}) \quad (8b)$$

$$c(r, z = \infty, t) = c_b + \Delta c \quad (\text{far-field}) \quad (8c)$$

$$c(r = \infty, z, t) = c_b + \Delta c \quad (\text{far-field}) \quad (8d)$$

$$c(r, z = 0, t) = c_b \quad \text{for } |r| \leq R(t) \quad (\text{crack boundary}) \quad (8e)$$

$$\frac{\partial c}{\partial z}(r, z = 0, t) = 0 \quad \text{for } |r| > R(t) \quad (\text{mirror symmetry}) \quad (8f)$$

Change of variables. We now apply the change of variables:

$$(\bar{r}, \bar{z}, \bar{t}) = \left(\frac{r}{R(t)}, \frac{z}{L}, \frac{t}{T} \right) \quad \text{and} \quad \bar{c} = \frac{c - c_b}{\Delta c} \quad (9)$$

We choose T as the total duration of the experiment, and the axial (along z) diffusion length-scale $L = \sqrt{DT}$. This change of variables only significantly affects the PDE (8a), and the boundary conditions (8e), (8f). The new system, in the reference frame moving with the crack, is

$$\frac{1}{DT} \left(\frac{\partial \bar{c}}{\partial \bar{t}} - T \frac{R'(t)}{R(t)} \bar{r} \frac{\partial \bar{c}}{\partial \bar{r}} \right) = \frac{1}{R^2(t)} \frac{1}{\bar{r}} \frac{\partial}{\partial \bar{r}} \left(\bar{r} \frac{\partial \bar{c}}{\partial \bar{r}} \right) + \frac{1}{L^2} \frac{\partial^2 \bar{c}}{\partial \bar{z}^2} \quad (10a)$$

$$\bar{c}(\bar{r}, \bar{z}, \bar{t} = 0) = 1 \quad (10b)$$

$$\bar{c}(\bar{r}, \bar{z} = \infty, \bar{t}) = 1 \quad (10c)$$

$$\bar{c}(\bar{r} = \infty, \bar{z}, \bar{t}) = 1 \quad (10d)$$

$$\bar{c}(\bar{r}, \bar{z} = 0, \bar{t}) = 0 \quad \text{for } |\bar{r}| \leq 1 \quad (10e)$$

$$\frac{\partial \bar{c}}{\partial \bar{z}}(\bar{r}, \bar{z} = 0, \bar{t}) = 0 \quad \text{for } |\bar{r}| > 1 \quad (10f)$$

Now, the boundary conditions are fixed, but the coefficients in (10a) are no longer constant. As a result, neither the original system nor this new system of equations can be solved analytically.

Scaling arguments. This new system is however well suited to analyse the relative importance of each term in (10a) using scaling arguments, as briefly explained in the main paper. Assuming $R(t) = \alpha t$ we obtain at our ‘final’ target time $t = T$ the following balance

$$\underbrace{\frac{\partial \bar{c}}{\partial \bar{t}} - \bar{r} \frac{\partial \bar{c}}{\partial \bar{r}}}_{O(1)} = \underbrace{\frac{1}{Pe} \frac{1}{\bar{r}} \frac{\partial}{\partial \bar{r}} \left(\bar{r} \frac{\partial \bar{c}}{\partial \bar{r}} \right)}_{\text{radial } O(Pe^{-1})} + \underbrace{\frac{\partial^2 \bar{c}}{\partial \bar{z}^2}}_{\text{axial } O(1)} \quad (11)$$

where we define the ‘final’ Péclet number as

$$Pe = \frac{R^2(T)}{L^2(T)} = \frac{\alpha^2 T}{D} = \frac{\alpha R_{\max}}{D}, \quad (12)$$

either using the maximum time T , or the maximum radius achieved $R_{\max} = \alpha T$.

Since all ‘bar’ variables and derivatives are of order one, (11) shows qualitatively that a final value $Pe \gg 1$ is a necessary (but not strictly sufficient) condition to neglect radial over axial diffusion, as we have done in the main paper.

Based on our extreme experimental values of α, R_{\max} , our minimum Péclet number is $Pe \approx 2 \cdot 10^{-5} \times 4 \cdot 10^{-3} / (2 \cdot 10^{-9}) \approx 40$, and our maximum is $Pe \approx 2 \cdot 10^{-4} \times 8 \cdot 10^{-3} / (2 \cdot 10^{-9}) \approx 800$.

Numerical simulations. To assess the quantitative errors associated with our lowest Pe values, the full system of equations (10) was solved numerically using Matlab’s PDE toolbox (the codes can be downloaded from the repository doi.org/10.17863/CAM.60212). The simulation parameters $\alpha = 10^{-5} \text{ ms}^{-1}$ and $T = 300 \text{ s}$ were chosen to give $Pe = 15$, a value two to three times lower than in any of our experiments, so as to provide a very conservative error estimate.

A visualisation of the results at the final time are shown in figure 6a, where we see that the region affected by diffusion does not extend much beyond the crack edge $|\bar{r}| \leq 1 \Leftrightarrow r < R(t)$, and that the axial gradients $|\partial_{\bar{z}} \bar{c}|$ are indeed much greater than the radial gradients $|\partial_{\bar{r}} \bar{c}|$.

More quantitatively, we focus on a single output variable of greatest interest: the volume flux through the crack surface. In the limiting case of fast growth ($Pe = \infty$) the one-dimensional axial diffusion model in the main paper provides an analytical expression to which we will compare the fully two-dimensional simulations. After applying the convolution integral taking into account the growth history (as explained in the main paper), this analytical flux is (in dimensional units)

$$\frac{dV}{dt} = \frac{8}{3} (\pi D_{\text{eff}})^{1/2} \alpha^2 t^{3/2} + \underbrace{2\pi R_0^2 D_{\text{eff}}^{1/2} t^{-1/2}}_{\approx 0}, \quad (13)$$

The second term vanishes assuming a small initial crack $R_0 = R(t=0) \approx 0$ (taken as 0.1 mm in the simulation).

The results in figure 6b show that:

- The numerical (fully two-dimensional) flux curve (in blue) is slightly above the analytical flux curve (13) (in red), as expected since radial diffusion adds to the overall transport. However at larger times both curves become indistinguishable.
- At $Pe = 15$, the final ($t = T = 300$) flux curves are less than 1% apart. This very small discrepancy is expected to be reduced

much further at the higher $Pe = 40 - 800$, which the main paper focuses on, hence our axial diffusion approximation is very comfortably confirmed.

- The overall functional dependence of the flux $\propto t^{3/2}$ is preserved, such that even at lower Péclet numbers (say $1 < Pe \lesssim 10$ for example), we would expect radial diffusion to merely change the pre-factor in our expression $\alpha = (64/25\pi) D S^2 \ell^{-1}$, but not the linear growth $R(t) = \alpha t$.

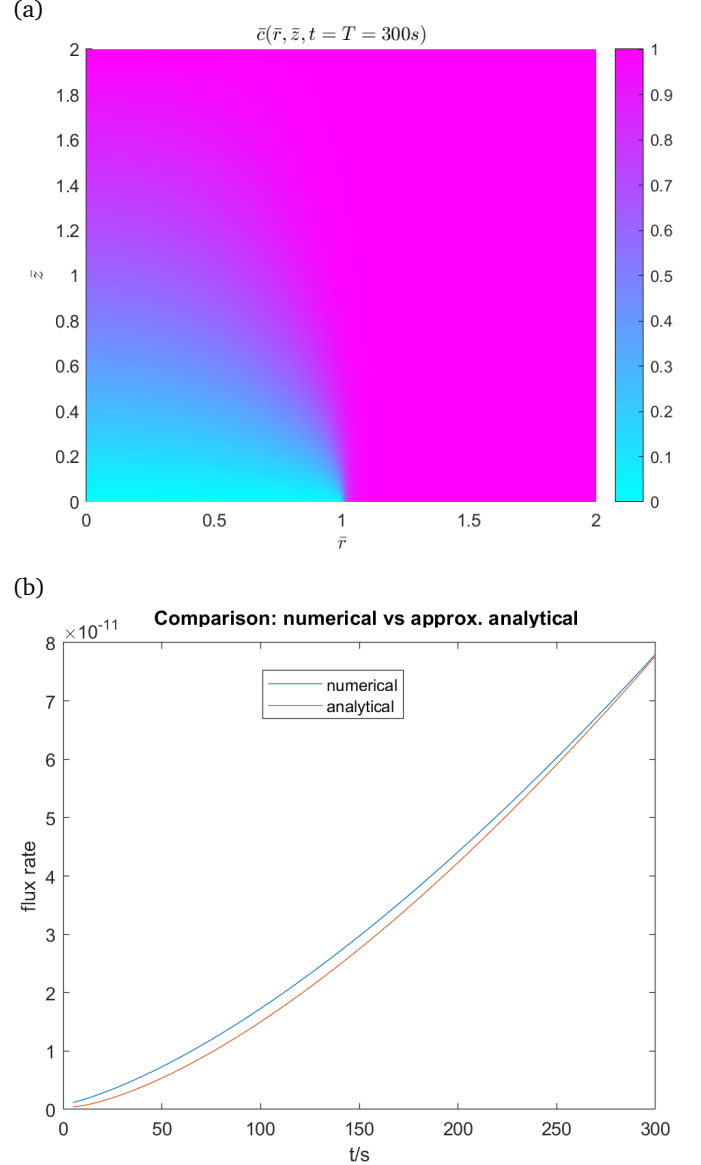


Fig. 6 Numerical solution of (10) for parameters corresponding to a growth that is very slow ($\alpha = 10^{-5} \text{ ms}^{-1}$) and long ($T = 300 \text{ s}$), equivalent to $R_{\max} = 3 \text{ mm}$ and $Pe = 15$. (a) Final dissolved gas concentration field (non-dimensional units) $\bar{c}(\bar{r}, \bar{z})$ at $t = T$ (i.e. $\bar{t} = 1$). A value of $\bar{c} = 1$ corresponds to $c = \Delta c = c_s - c_b$, the far-field excess concentration compared to the boundary. (b) Volume flux dV/dt across the growing crack (in $\text{m}^3 \text{ s}^{-1}$): comparison between numerical result (blue) and $Pe = \infty$ analytical (13) (red). Agreement is almost perfect at the target time $T = 300$.

Notes and references

- 1 S. Karthika, T. Radhakrishnan and P. Kalaichelvi, *Crystal Growth & Design*, 2016, **16**, 6663–6681.
- 2 L. D. Landau and E. M. Lifshitz, *Theory of Elasticity*, Pergamon Press (English), 2nd edn, 1970.
- 3 P. Patriccio, *American Journal of Physics*, 2004, **72**, 1488–1491.
- 4 X. Zhao, N. Huebsch, D. J. Mooney and Z. Suo, *Journal of Applied Physics*, 2010, **107**, 063509.
- 5 G. Bradski, *Dr. Dobb's Journal of Software Tools*, 2000.
- 6 B. Hammel and N. Sullivan-Molina, *bdhammel/least-squares-ellipse-fitting: v2.0.0*, 2020, <https://doi.org/10.5281/zenodo.3723294>.
- 7 W. C. Karl, G. C. Verghese and A. S. Willsky, *CVGIP: Graphical Models and Image Processing*, 1994, **56**, 124–139.
- 8 P. Virtanen, R. Gommers, T. E. Oliphant, M. Haberland, T. Reddy, D. Cournapeau, E. Burovski, P. Peterson, W. Weckesser, J. Bright, S. J. van der Walt, M. Brett, J. Wilson, K. J. Millman, N. Mayorov, A. R. J. Nelson, E. Jones, R. Kern, E. Larson, C. J. Carey, Í. Polat, Y. Feng, E. W. Moore, J. VanderPlas, D. Laxalde, J. Perktold, R. Cimrman, I. Henriksen, E. A. Quintero, C. R. Harris, A. M. Archibald, A. H. Ribeiro, F. Pedregosa, P. van Mulbregt and SciPy 1.0 Contributors, *Nature Methods*, 2020, **17**, 261–272.